energies

MDPI

Article

Investigation of the Discharge Characteristics Induced by Free Metallic Particles on Insulation Surfaces Under Low-Pressure Conditions

Wei Wang [1,*], Yinzhang Cheng [1], Xueting Bai [1], Zhenyu Lu [1], Kai Zhang [1], Yu Liu [1], Zhixiang Liu [1] and Zhipeng Lei [2,*]

[1] State Grid Shanxi Electric Power Company Electric Power Research Institute, Taiyuan 030012, China
[2] College of Electrical and Power Engineering, Taiyuan University of Technology, Taiyuan 030024, China
* Correspondence: sxdkwangweidyk@163.com (W.W.); leizhipeng@tyut.edu.cn (Z.L.)

Abstract

Metallic particles attached to epoxy resin surfaces can severely distort the local electric field, degrade surface-insulation reliability, and reduce the partial discharge inception voltage (PDIV), partial discharge extinction voltage (PDEV), and flashover voltage (FOV). These adverse effects become more pronounced under low-pressure conditions. To investigate the discharge mechanism of metallic particles on epoxy resin surfaces in high-altitude, low-pressure environments and to assess the effectiveness of conventional online partial discharge (PD) monitoring methods for detecting metallic-particle defects, a low-pressure surface discharge test platform was developed. The motion and discharge behaviors of metallic particles subjected to an electric field were recorded under both atmospheric and reduced-pressure conditions. The PDIV, PDEV, and FOV were systematically measured for epoxy resin specimens with and without metallic particles. In addition, the responses of ultrasonic, transient earth voltage (TEV), and ultra-high-frequency (UHF) sensors to metallic-particle-induced discharges were evaluated. The results showed that, under low-pressure conditions, metallic particles substantially reduced the PDIV, PDEV, and FOV of epoxy resin surface insulation. They also altered the dominant flashover behavior. All three sensing methods can effectively detect discharges caused by free metallic particles, whereas the ultrasonic signal is attenuated as the air pressure decreases.

Keywords: epoxy resin; metallic particles; low pressure; partial discharge; surface flashover; electric-field distortion; online monitoring

Check for updates

Academic Editor: Constantinos S. Psomopoulos

Received: 5 September 2026
Revised: 11 October 2026
Accepted: 14 October 2026
Published: 19 October 2026

Copyright: © 2026 by the authors. Licensee MDPI, Basel, Switzerland. This article is an open access article distributed under the terms and conditions of the Creative Commons Attribution (CC BY) license.

1. Introduction

Owing to its superior electrical insulation performance, high mechanical strength, and good environmental adaptability, epoxy resin is extensively employed as a supporting and insulating material in electrical equipment, including gas-insulated switchgear (GIS), gas-insulated transmission lines (GIL), and cast-resin transformers [1–3]. Nevertheless, conductive foreign matter, such as metallic particles, metal dust, and burrs, may be introduced or generated during equipment manufacturing, transportation, installation, and operation. When metallic particles adhere to an epoxy resin surface or enter a high-field region, they can strongly distort the local electric field and facilitate charge injection and partial-discharge propagation. Under severe conditions, these effects can accelerate surface degradation and ultimately trigger surface flashover [4,5].

As the air pressure decreases from standard atmospheric pressure (101.3 kPa) to below 50 kPa, the breakdown strength of air can decrease by approximately 30–50%, leading to pronounced reductions in the PDIV and FOV [6,7]. The reduced gas density under low-pressure conditions modifies the electron mean free path and collision-ionization processes, thereby significantly affecting the PDIV, PDEV, and FOV. Previous work has shown that, over the pressure range of 20–60 kPa, the surface PDIV and breakdown voltage of epoxy resin exhibit an overall decreasing trend with decreasing pressure [8]. Moreover, both reduced pressure and airflow can substantially modify the discharge morphology and inception threshold of surface discharges along insulating materials [9]. Studies on aircraft wiring, motor insulation, and printed circuit boards have likewise confirmed that a decrease in air pressure increases the susceptibility to PD and modifies the associated discharge thresholds, phase-resolved characteristics, and aging behavior [10–13]. Investigations of different polymeric insulating materials have further demonstrated that reduced pressure alters the distributions of surface charge and electron density, which in turn influences the propagation and evolution of surface discharges [14,15]. Consequently, minor defects that pose little risk under normal atmospheric conditions may become critical discharge-initiation sites at low pressure and eventually trigger partial discharge or surface flashover.

Research on metallic-particle defects in insulation systems has focused primarily on particle motion, local electric-field distortion, and the associated discharge behavior. Multiscale dynamic analyses and studies involving different electrode surface conditions have shown that adhesion, rebound, and adsorption after particle–insulator collisions, together with particle charging processes, can substantially alter particle dynamics and the surrounding electric-field distribution [16,17]. In addition, the collective motion and discharge activity of multiple particles under AC electric fields can exacerbate local electric-field distortion near the insulator surface [18].

With regard to metallic-particle-induced surface discharges, Jiang et al. established a numerical model to characterize discharge development along insulating surfaces and analyzed the effects of particle-induced local electric-field enhancement and surface charge accumulation [19]. Chen et al. experimentally and numerically investigated metallic-particle defects on epoxy resin surfaces using two-dimensional simulations. Their results showed that PD activity was predominantly localized at the particle extremities and the metal–epoxy resin–air triple junction, and that repetitive discharges could progressively damage the insulation surface [20]. Sakai et al. demonstrated that free wire-like metallic particles subjected to an AC electric field tend to migrate toward high-field regions and may exhibit pronounced discharge activity at their ends [21]. Subsequent investigations have revealed that both the dimensions and spatial locations of metallic particles strongly influence their PD characteristics and detectability [22]. The detection probability of latent metallic-particle defects can be enhanced by mechanical excitation [23]. Moreover, metallic contamination defects on insulator surfaces may undergo a progressive transition from intermittent discharges to sustained discharge activity and ultimately to insulation breakdown under continuous voltage stress [24].

For PD condition monitoring, pulse-current, ultrasonic, transient earth voltage (TEV), and ultra-high-frequency (UHF) techniques have been extensively employed for detecting insulation defects in electrical equipment. In recent years, multimodal sensing based on multiple physical quantities has emerged as an effective means of enhancing the reliability of PD detection. Typical approaches include integrated UHF and gas-condition monitoring [25], optical–UHF data fusion [26], and UHF-synchronized ultrasonic PD detection [27]. Han et al. further developed a combined TEV–ultrasonic sensing technique capable of detecting, diagnosing, and locating PDs in switchgear [28]. Previous studies have also shown that TEV sensors can capture high-frequency components associated with PDs in

epoxy insulation, with the extracted signal features providing information on the evolution of surface erosion and electrical treeing [29]. Nevertheless, most existing investigations of metallic-particle defects have been conducted under normal atmospheric pressure or in pressurized-gas environments. By contrast, studies under low-pressure conditions have predominantly addressed conventional gas–solid interfaces without pronounced metallic defects or insulation systems intended for aerospace applications. Consequently, the discharge evolution characteristics of metallic-particle defects on epoxy resin surfaces at low pressure have not yet been systematically elucidated. Furthermore, how changes in air pressure affect the responses and applicability of conventional pulse-current, ultrasonic, TEV, and UHF monitoring techniques for such defects remains insufficiently understood.

To fill the aforementioned research gaps, this work investigates metallic-particle defects on epoxy resin surfaces under low-pressure air conditions. A pressure-controlled surface discharge test platform was developed to comparatively characterize the PDIV, PDEV, and FOV of epoxy resin specimens with and without metallic particles over a range of air pressures. A high-speed imaging technique was used to capture the motion of metallic particles under an applied electric field. In parallel, a finite-element model was developed to quantify particle-induced distortion of the local electric field on the epoxy resin surface. PD signals and phase-resolved partial-discharge (PRPD) patterns were also acquired using pulse-current, ultrasonic, TEV, and UHF techniques. These measurements enabled comparison of the sensor responses to metallic-particle defects under reduced-pressure conditions. The objective of this study is to clarify the discharge evolution and dynamic behavior of metallic particles on epoxy resin surfaces at low pressure and to evaluate the effectiveness of conventional online monitoring techniques for detecting such defects. The results are expected to provide a theoretical and experimental basis for insulation design and condition monitoring of electrical equipment operating in complex high-altitude environments.

2. Materials and Methods

2.1. Test Specimens

Planar specimens made of epoxy resin, Pelim EP6101, 71electric, Quzhou, China, were employed in this study, with dimensions of 215 mm × 150 mm × 4 mm. Before each test, the specimen surfaces were thoroughly cleaned using a trisodium phosphate solution to remove residual mold-release agents and grease. The specimens were subsequently rinsed with deionized water and completely dried before testing.

To achieve a balance between engineering representativeness and the observability of particle dynamics, two typical metallic-particle geometries were selected: spherical and wire-like particles. The spherical particle consisted of an aluminum sphere with a radius of 1 mm, while the wire-like particle consisted of an aluminum wire with a radius of 0.5 mm and a length of 10 mm. These dimensions were selected to approximate metallic contaminants found in power equipment while allowing their field-driven motion to be resolved by high-speed imaging. Because the aluminum wires were fabricated by cutting, their ends were appropriately polished before testing to avoid excessively sharp tips that could introduce additional electric-field enhancement.

2.2. Experimental Platform

Figure 1 illustrates the multi-physical-parameter detection platform developed for surface discharge experiments on epoxy resin under low-pressure conditions, in which the pulse-current method was used as the reference measurement.

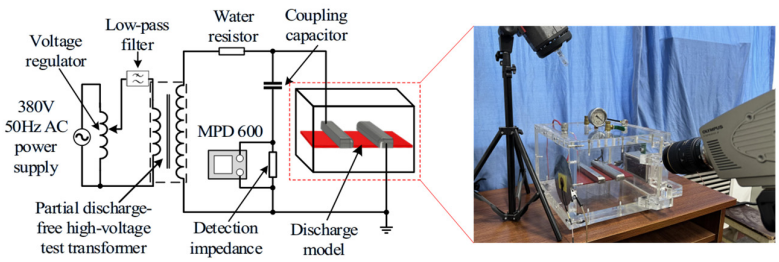


Figure 1. Multi-physical-parameter detection Platform.

A 380 V, 50 Hz AC source was used to energize the experimental system. A low-pass filter was incorporated to suppress power-supply interference, while the output voltage of a partial-discharge-free high-voltage test transformer was controlled by a voltage-regulating unit. A 20 kΩ water resistor served as a protective resistor to limit the transient overcurrent generated during flashover. The epoxy resin specimen was placed inside an acrylic vacuum chamber, in which the air pressure was controlled by evacuating the chamber using a vacuum pump. The gap between the high-voltage electrode and the grounded electrode was maintained at 4.5 cm, producing an approximately uniform electric field along the specimen surface. A coupling capacitor was employed to decouple the high-voltage source from the measurement branch while coupling the PD pulses into the detection circuit. Pulse-current measurements were performed using an MPD 600, OMICRON electronics GmbH, Klaus, Austria, PD measurement system, in which the discharge signals were acquired from the voltage response across the measuring impedance. The motion of the metallic particles under the applied electric field was recorded using an i-SPEED 3 high-speed camera, OLYMPUS, Essex, United Kingdom.

Owing to the 30-mm-thick acrylic wall of the vacuum chamber, ultrasonic waves were strongly attenuated and could not be effectively transmitted through the chamber wall. By contrast, electromagnetic signals experienced negligible attenuation when propagating through the acrylic enclosure. Accordingly, an air-coupled ultrasonic sensor was installed inside the vacuum chamber, and its output was routed outside through two silver-plated signal wires, each with an outer diameter of 0.38 mm, via a rubber-sealed feedthrough. The custom-made TEV sensor consisted of a copper electrode and a 1-mm-thick glass-fiber-reinforced epoxy resin substrate, whereas the UHF sensor employed a bow-tie antenna configuration. Both sensors were mounted externally on the vacuum chamber. The AC voltage reference signal and the outputs of the ultrasonic, TEV, and UHF sensors were synchronously recorded using a HDO6104 oscilloscope, Teledyne LeCroy, Chestnut Ridge, NY, United States, thereby ensuring temporal alignment among the signals acquired by the different sensing methods.

The air-coupled ultrasonic sensor had a center frequency of 40.0 ± 1.0 kHz, a bandwidth of 1.2 kHz, and a directivity angle of 50 ± 10°. Its output was amplified using a CTS-8682B amplifier, Guangdong Goworld Co., Ltd., Shantou, China, with a gain of 30 dB over the frequency range of 20–200 kHz before being connected to the oscilloscope.

The TEV sensor had a detection frequency range of 3–100 MHz and a voltage detection range of −20 to +20 V. A grounded galvanized stainless-steel disk with a radius of 75 mm and a thickness of 0.8 mm was attached to the outer surface of the acrylic chamber to provide the counter-electrode for capacitive coupling. The measured equivalent capacitance of the disk–TEV sensor assembly was approximately 0.1 nF. The bow-tie UHF sensor had a detection frequency range of 300–1500 MHz and an effective height of at least 10 mm.

The TEV and UHF sensors were connected directly to the oscilloscope through radio-frequency signal cables. The acquired waveforms were subsequently processed using

second-order Butterworth high-pass filters with cutoff frequencies of 3 MHz for TEV and 50 MHz for UHF. Forward–backward filtering was performed using the filter function to avoid introducing a net phase shift.

The simulation model of the metal-particle-induced discharge defect is illustrated in Figure 2. Table 1 reports the Material parameters of the model. In the model, the red region was assigned epoxy resin, while copper was specified as the material for both the high-voltage and grounded electrodes. The remaining domain was filled with air. The dimensions of the air domain were consistent with the internal dimensions of the vacuum chamber, and electrical insulation boundary conditions were applied to its outer boundaries. A user-controlled mesh with an extremely fine element size was employed. Given the critical role of the triple-junction region formed by the metal electrode, epoxy resin, and air, the minimum mesh element size in this region was set to 0.1 mm to improve the spatial resolution of the electric field distribution. A power-frequency AC voltage of 15 kV was applied to the high-voltage electrode. A transient study was conducted to investigate the electric field distribution on the epoxy resin surface at different time instants under the parallel-plate electrode configuration. The time step was set to 0.5 ms, and the transient electric field was calculated over one complete power-frequency cycle.

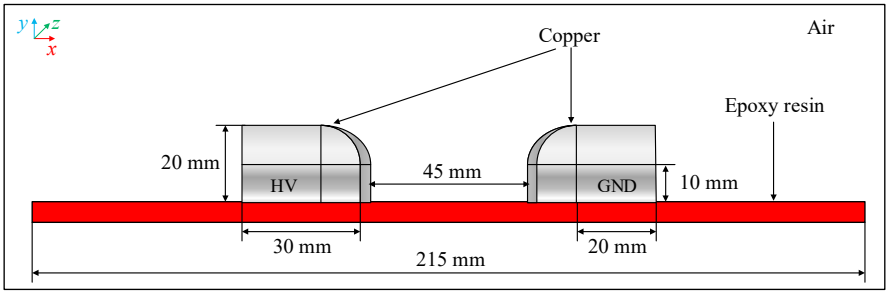


Figure 2. Geometry and dimensions of the simulation model.

Table 1. Material parameters.

Material	Conductivity (S/m)	Relative Permittivity
Epoxy resin	5×10^{-15}	4.5
Copper	5.9×10^{7}	1
Aluminum	3.774×10^{7}	1
Air	0	1

2.3. Experimental Method

During PDIV measurements, the metallic particle was initially positioned on the epoxy resin surface between the high-voltage and grounded electrodes. A spirit level was used to adjust the specimen horizontally, thereby minimizing the influence of slight surface inclination on particle dynamics. To better represent the various orientations of metallic wires that may occur in practical equipment and to evaluate their influence on insulation performance, three typical initial orientations were investigated. Specifically, the angle between the longitudinal axis of the metallic wire and the electric-field direction of the quasi-uniform field was set to 0°, 45°, and 90°, respectively. Figure 3 shows the metallic-particle defect discharge configuration for the representative case in which the wire axis is aligned with the electric-field direction (0°).

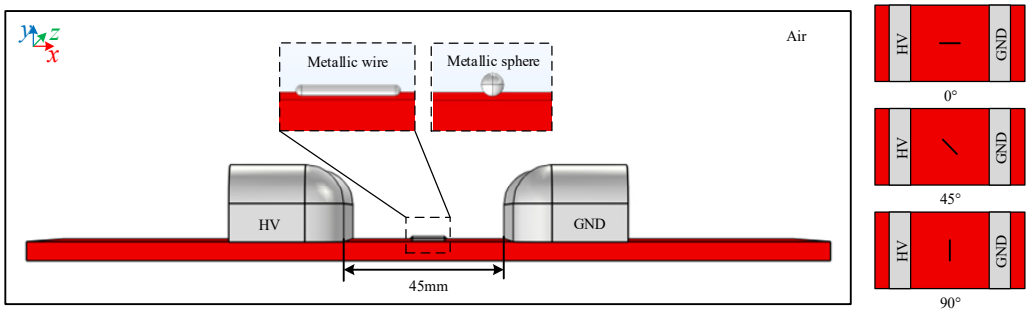


Figure 3. Discharge model.

The chamber pressure was subsequently adjusted to the prescribed value. An AC voltage was then applied across the electrodes and ramped at approximately 200 V/s. The voltage at which the apparent charge measured by the pulse-current method first exceeded 100 pC was taken as the PDIV for the corresponding pressure condition. The FOV was determined using a similar voltage-application procedure, with the ramp rate increased to approximately 300 V/s. Meanwhile, particle motion was recorded by a high-speed camera positioned at a 45° oblique angle relative to the specimen surface, operating at 500 frames/s.

All experiments were conducted at an ambient temperature of 20 ± 5 °C and a relative humidity of 45 ± 5%. According to the China Meteorological Administration, the annual mean atmospheric pressure at the laboratory site is approximately 92.6 kPa (0.91 atm). The test pressure was progressively reduced from the local atmospheric pressure to approximately 22.6 kPa at intervals of approximately 10 kPa. At each pressure level, the PDIV, PDEV, and FOV were measured five times for each of three representative surface conditions: an epoxy resin surface without metallic particles, with a spherical aluminum particle, and with a wire-like aluminum particle. Meanwhile, the motion processes of spherical and wire-like metallic particles were synchronously recorded using a high-speed camera, and their motion behaviors under identical pressure and initial configuration conditions were compared.

The pressure stability of the vacuum chamber was experimentally verified before electrical testing. After the chamber pressure reached its preset value, no significant pressure variation was observed within 1 h. Following the onset of PD, the chamber pressure increased by no more than 5% of the preset value within 10 min. Accordingly, each PDIV test was completed within 3 min to ensure that the influence of pressure drift remained negligible. A single flashover event resulted in a maximum pressure increase of less than 10% relative to the preset pressure. Because the FOV was acquired instantaneously at the occurrence of flashover, the subsequent pressure deviation had no appreciable influence on the measurement.

Since PD activity and surface flashover could cause displacement of the metallic particles, the particles were repositioned after each test such that they were equidistant from the two electrodes. Furthermore, because surface flashover can erode the epoxy resin and alter its surface insulation characteristics, sufficient time was allowed after each test for residual surface charges to dissipate. The epoxy resin specimen was replaced after each flashover test to prevent flashover-induced surface deterioration from affecting subsequent measurements.

3. Results

3.1. Electric-Field Distribution Characteristics

In the simulation model, a 15 kV, 50 Hz AC voltage was applied between the electrodes. Figure 4 presents the resulting electric-field distributions on the epoxy resin surface for

three configurations: particle-free, with a spherical metallic particle, and with a wire-like metallic particle.

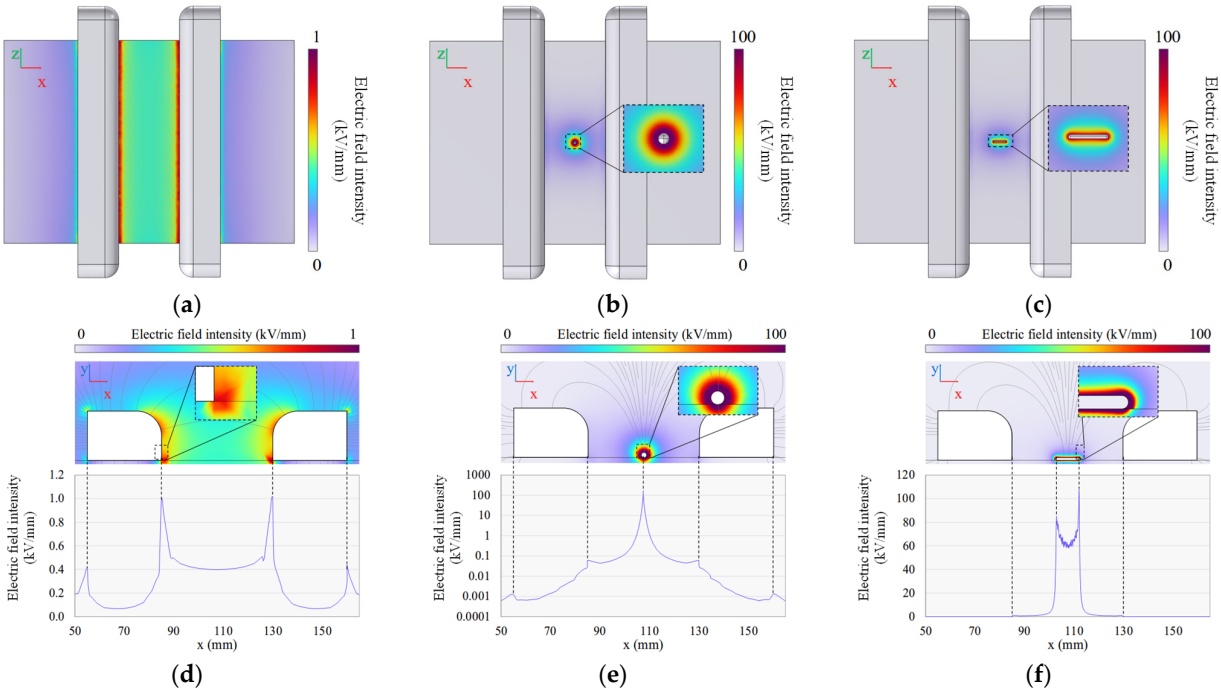
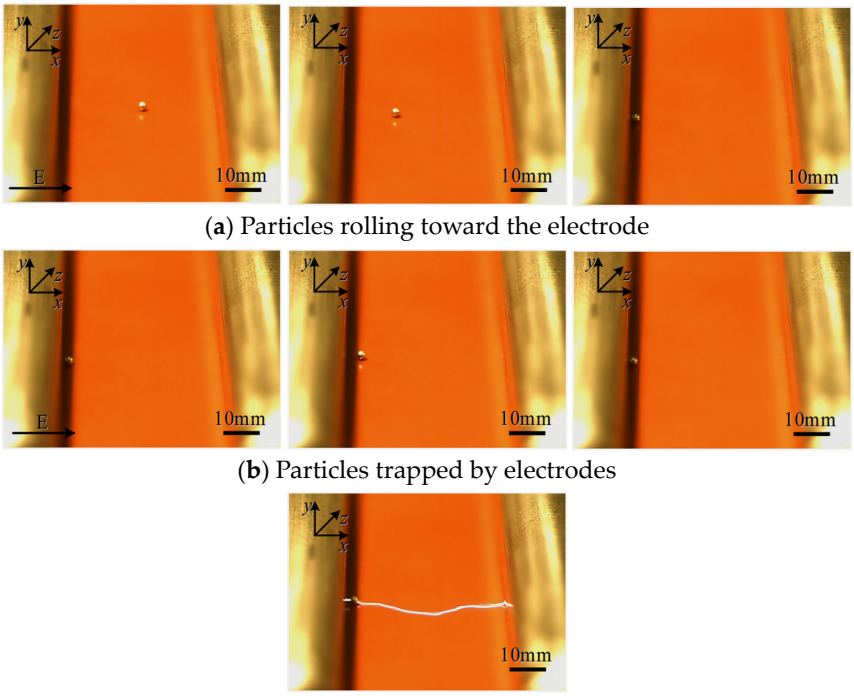


Figure 4. Electric field distribution: (**a**) Top view without metal particles; (**b**) Top view of spherical metal particles; (**c**) Top view of wire like metallic particles; (**d**) Side view without metal particles; (**e**) Side view of spherical metal particles; (**f**) Side view of wire like metallic particles.

Figure 4 demonstrates that metallic particles introduce pronounced local electric-field enhancement on the epoxy resin surface. For the spherical particle, the peak electric-field intensity appears at the metal–epoxy resin–air triple junction beneath the sphere and is approximately 167.28 times higher than that under the particle-free condition. In the case of the wire-like particle, the peak field is concentrated at the wire-tip–epoxy resin–air triple junction, reaching approximately 106.66 times the corresponding value without metallic particles.

3.2. Dynamic Behavior of Metallic Particles

Figure 5 illustrates the motion of a spherical metallic particle under electric-field excitation. Based on repeated observations, PD is first initiated on the epoxy resin surface as the applied voltage is increased. With increasing voltage, the metallic sphere begins to roll toward the closer electrode and is eventually confined to the region near that electrode. Thereafter, it undergoes a repetitive repulsion-and-attraction motion within a limited range. At a still higher voltage, a flashover channel originates from one electrode, extends toward and passes through the region occupied by the metallic sphere, and subsequently propagates along the epoxy resin surface to the opposite electrode, resulting in a complete surface flashover.



(**a**) Particles rolling toward the electrode

(**b**) Particles trapped by electrodes

(**c**) Flashover along particles

Figure 5. Dynamic behavior of spherical metal particles (**a**) Particles rolling toward the electrode; (**b**) Particles trapped by electrodes; (**c**) Flashover along particles.

Reducing the air pressure does not alter the temporal sequence between PD inception and the onset of rolling motion of the spherical metallic particle. Although the spherical geometry results in relatively low mechanical resistance to rolling, substantial electric-field enhancement occurs at the metal–epoxy resin–air triple junction beneath the particle. Consequently, the local electric field can reach the threshold for PD inception at a voltage lower than that required to generate sufficient electrostatic force to initiate particle motion. Therefore, during voltage escalation, PD occurs before the spherical particle begins to roll, and this sequence remains unchanged under low-pressure conditions.

Compared with spherical particles, wire-like metallic particles exhibit considerably more complex dynamic behavior under electric-field excitation. Figure 6 summarizes four typical motion modes of a wire-like particle viewed in the x–z plane. The electrodes depicted on the left and right sides are included solely to indicate their positions relative to the metallic wire; their locations do not correspond to the high-voltage and grounded terminals, respectively.

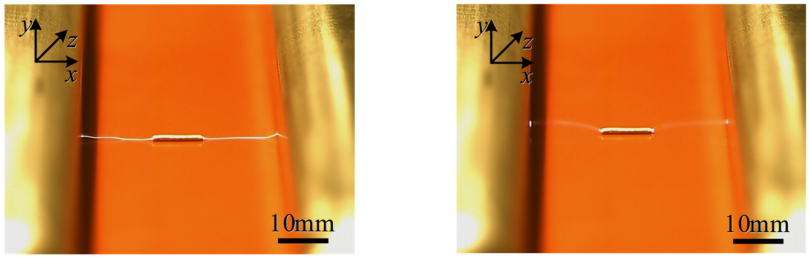


(**a**) Slight deflection I (**b**) 90° deflection (**c**) Slight deflection II (**d**) Diagonal movement

Figure 6. Typical motion characteristics of wire-like metallic particles. (**a**) Slight deflection I; (**b**) 90° deflection; (**c**) Slight deflection II, and (**d**) Diagonal movement.

For an initial wire orientation of 0° relative to the electric-field direction, PD is initiated first as the applied voltage increases, after which the metallic wire exhibits small-amplitude reciprocating rolling. Because of the relatively large contact area between the wire and the

epoxy resin surface, the resulting static friction is sufficiently high that the electrostatic force remains inadequate to transport the wire toward the electrode. As illustrated in Figure 7, once the applied voltage reaches a critical level, the wire acts as a conductive bridge that facilitates the development of the flashover channel. The discharge path extends along the epoxy resin surface via the metallic wire and ultimately bridges the two electrodes. Afterward, the hot discharge channel rises away from the insulation surface under thermal buoyancy and gradually extinguishes in the surrounding air.



(**a**) Surface flashover (**b**) Flashover channel floating up

Figure 7. Surface flashover with a wire-like metallic particle initially oriented at 0° (**a**) Surface flashover; (**b**) Flashover channel floating up.

When the wire-like metallic particle is initially oriented at 45° with respect to the electric-field direction, it tends to rotate, as shown in Figure 6a, until its longitudinal axis becomes nearly parallel to the field lines as the applied voltage increases. Once aligned, the particle exhibits slight reciprocating rolling, and the associated PD intensifies rapidly. As the voltage is further increased, surface flashover is eventually initiated along the epoxy resin surface. During the rotational process, there is also a certain probability that the particle will roll obliquely toward the nearer electrode.

Figure 8 shows that when the metallic wire is located close to one electrode, a streamer channel is first established between the electrode and the adjacent end of the wire. The discharge path then extends further from the far end of the wire toward the opposite electrode, thereby forming a continuous flashover path and initiating flashover.

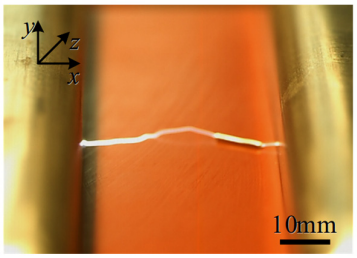


Figure 8. 45° wire-like metallic particle flashover.

Contact between the metallic wire and an electrode effectively extends the electrode boundary and abruptly shortens the effective interelectrode gap. In combination with the pronounced field enhancement at the distal end of the particle, this configuration is highly favorable for the initiation of surface flashover. Nevertheless, repeated tests revealed that a fully developed streamer path invariably formed before direct particle–electrode contact. This behavior can be attributed to the strong local field arising from polarization-charge accumulation at the particle tip and the electrostatic induction between the approaching wire and the electrode. These combined effects are sufficiently strong to induce breakdown of the remaining gas gap prior to mechanical contact.

Because an exactly perpendicular orientation between the wire axis and the electric field cannot be realized experimentally, a wire initially arranged at approximately 90° is

still subjected to an electric torque and therefore undergoes rotational motion. Depending on the instantaneous force and torque conditions, the particle may roll toward an electrode, as illustrated in Figure 6d, or rotate locally without pronounced translational displacement, as shown in Figure 6c. A relatively large electric torque is required to rotate a wire from an orientation close to 90°, and thus this motion generally occurs at a higher applied voltage. Consequently, irrespective of the specific trajectory, once the wire approaches or contacts an electrode or becomes approximately aligned with the electric-field direction, the combined effects of the sharply reduced effective electrode spacing and enhanced tip field can rapidly initiate surface flashover.

A reduction in air pressure modifies the sequence between particle motion and discharge development for wire-like metallic-particle defects on epoxy resin surfaces. The most prominent changes are the advancement of flashover initiation and the alteration of streamer propagation behavior.

For a wire initially oriented at approximately 45° to the electric-field direction, rotation or rolling precedes flashover at ambient pressure. In contrast, when the pressure decreases below 42.6 kPa, the continuous streamer channel shown in Figure 9 develops before any observable rotational or rolling motion of the particle. Similar behavior occurs for an initial orientation of approximately 90°. Rather than forming only after the wire has rotated into alignment with the electric field, the streamer channel develops while the particle is still rotating. More importantly, the discharge path changes from surface-guided propagation to direct gas-gap breakdown, producing a faint-purple streamer channel in the air above the epoxy resin surface. Although its appearance resembles the buoyancy-driven upward arc observed after surface flashover at atmospheric pressure, the underlying development process is fundamentally different. Under low-pressure conditions, the discharge channel originates directly within the gas gap, whereas at atmospheric pressure it initially propagates along the epoxy resin surface and only subsequently rises into the surrounding air owing to thermal buoyancy.

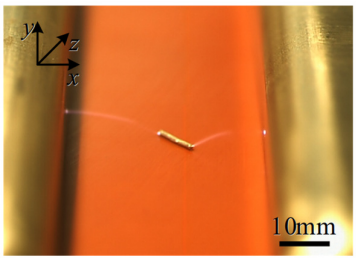


Figure 9. Low pressure wire-like metallic particle flashover.

This phenomenon may be related to microscopic surface irregularities at the ends of the wire-like particles. With decreasing air pressure, the electron mean free path increases, making electron acceleration and impact ionization more favorable within the high-field region surrounding the particle tip. As a result, the gas-phase path between the particle tip and the electrode may have a lower effective breakdown threshold than the competing creepage path along the dielectric surface. The discharge therefore preferentially develops through the gas gap rather than along the epoxy resin surface.

3.3. Discharge Characteristics

Figure 10a presents the pressure dependence of the PDIV, PDEV, and FOV for an epoxy resin surface containing a spherical metallic particle. All three characteristic voltages decrease monotonically as the air pressure is reduced from 92.6 to 22.6 kPa. The PDIV shows the strongest pressure dependence, decreasing from an average of 9.12 kV at ambient pressure to 4.41 kV at 22.6 kPa, corresponding to a reduction of approximately 51.6%.

In comparison, the FOV decreases from 20.6 to 15.77 kV over the same pressure range, corresponding to a more moderate reduction of approximately 23.4%.

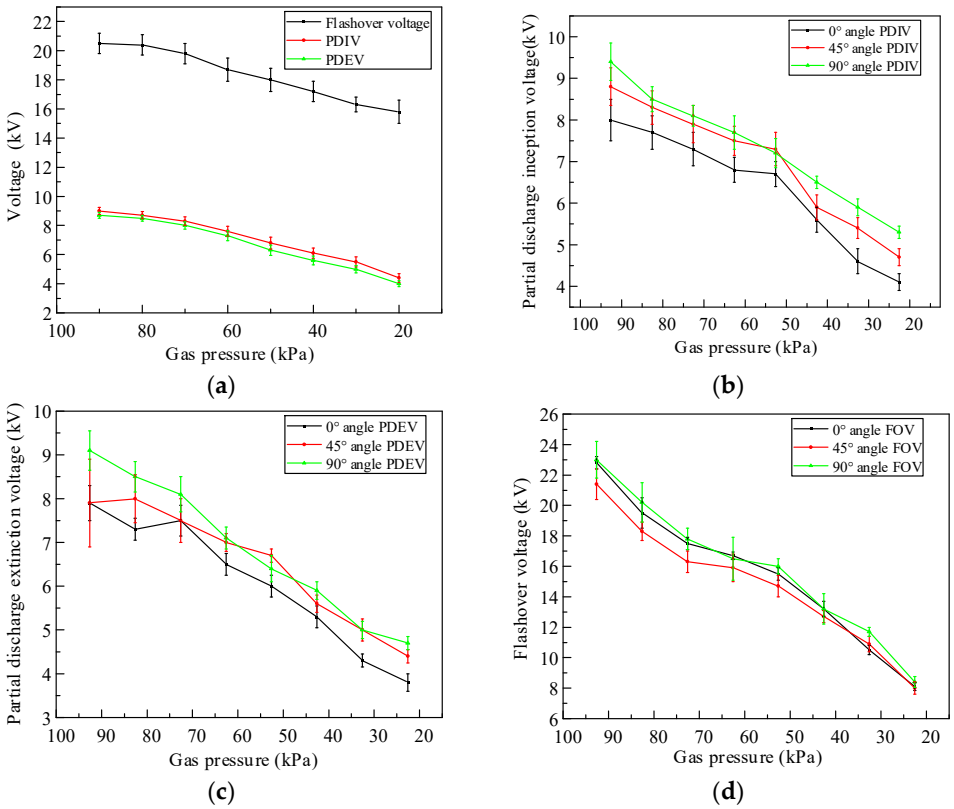


Figure 10. Pressure dependence of the discharge characteristic voltages for spherical and wire-like metallic particles (**a**) PDIV, PDEV, and FOV of spherical metal particles; (**b**) PDIV of wire-like metallic particles; (**c**) PDEV of wire-like metallic particles; (**d**) FOV of wire-like metallic particles.

According to the simulation results, PD inception is primarily governed by the strongly enhanced electric field near the metal sphere–epoxy resin–air triple junction beneath the spherical particle. Reducing the air pressure modifies the ionization processes within this high-field region and therefore lowers the applied voltage required for discharge inception. This interpretation is consistent with Figure 10a, which shows a progressive reduction in the critical electric-field intensity for PD inception as the pressure decreases. At the same time, the increase of extinction coefficient also indicates that the self-sustaining ability of partial discharge becomes stronger at low pressure, and it needs lower voltage to extinguish after occurrence.

The flashover process, however, is dominated by the particle dynamics after the metallic sphere has migrated to and become confined near the electrode. The repetitive motion of the sphere in this region is governed mainly by electric forces. Although reduced air pressure decreases aerodynamic resistance, it has only a limited effect on the motion of the spherical particle. PD inception is strongly controlled by gas ionization, whereas the subsequent particle motion is less sensitive to pressure. Consequently, the FOV of the spherical-particle configuration depends less strongly on air pressure than does the PDIV.

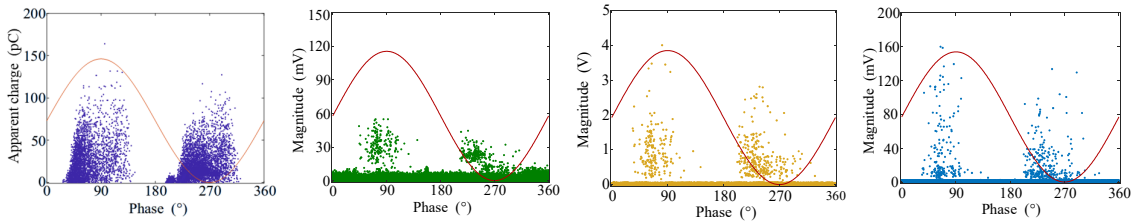
For wire-like metallic particles, Figure 10 compares the PDIV, PDEV, and flashover voltage as functions of pressure for three initial orientations relative to the electric field. Similar to the spherical-particle results, all three characteristic voltages decrease approximately linearly with decreasing air pressure. In general, both the PDIV and PDEV follow the order 90° > 45° > 0°. The only exception occurs at 92.6 kPa, where rotation of the

particle initially oriented at 45° causes its PDEV to become approximately equal to that measured for the 0° orientation.

In contrast to the PDIV and PDEV, the FOV shows a distinct dependence on the initial orientation of the wire-like particle. For the 45° configuration, the particle rotated or rolled before flashover across most of the investigated pressure range, resulting in the lowest flashover voltage among the three initial orientations. Moreover, inclined wire configurations exhibit greater stochasticity in particle dynamics. This increased uncertainty leads to a larger dispersion of the FOV measured at a given pressure.

3.4. Phase-Resolved PD Characteristics

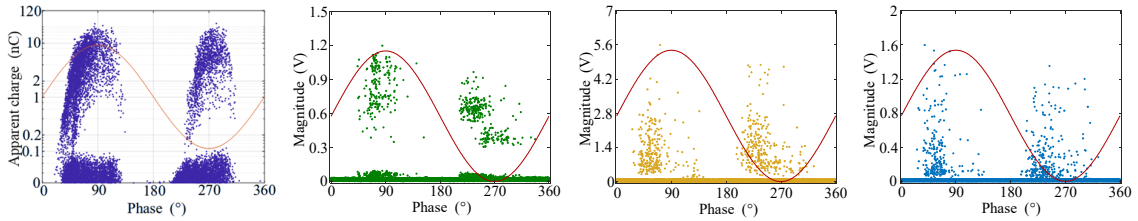
Figure 11 shows the PRPD pattern obtained for a spherical metallic-particle defect at an applied voltage of 9.5 kV under ambient-pressure conditions. The discharge distribution is approximately symmetric with respect to the positive and negative half-cycles of the AC voltage. PD pulses are predominantly distributed over the rising and falling portions of both half-cycles, displaying phase-resolved characteristics similar to those typically associated with surface discharges. Such symmetry can be attributed primarily to the highly symmetric geometry of the spherical metallic particle.



(**a**) Pulse-current (**b**) Ultrasonic (**c**) TEV (**d**) UHF

Figure 11. PRPD pattern of spherical metallic-particle defects at 92.6 kPa and 9.5 kV (**a**) Pulse-current; (**b**) Ultrasonic; (**c**) TEV; (**d**) UHF.

Figure 12 presents the discharge characteristics during the stable PD stage after the metallic sphere migrated toward the nearer electrode. The PRPD pattern in Figure 12a reveals two clearly separated discharge populations in terms of apparent charge magnitude. Because the pulse amplitudes span several orders of magnitude, a logarithmic scale is used for the vertical axis. Two distinct pulse clusters can be identified in each polarity half-cycle. The high-amplitude cluster extends approximately from 100 pC to 60 nC and shows a pronounced dependence on the instantaneous power-frequency voltage. The low-amplitude cluster, by contrast, is densely concentrated below 100 pC and exhibits a distribution similar to that observed near PD inception. These characteristics suggest the coexistence of two discharge sources. The low-amplitude population is primarily associated with discharge activity at the metal sphere–epoxy resin–air triple junction beneath the particle, whereas the high-amplitude population originates mainly from surface discharge paths between the metallic sphere and the adjacent electrodes. Since the sphere is trapped in the vicinity of one electrode, the spatial asymmetry of the discharge configuration results in an asymmetric distribution of the high-amplitude pulse cluster.

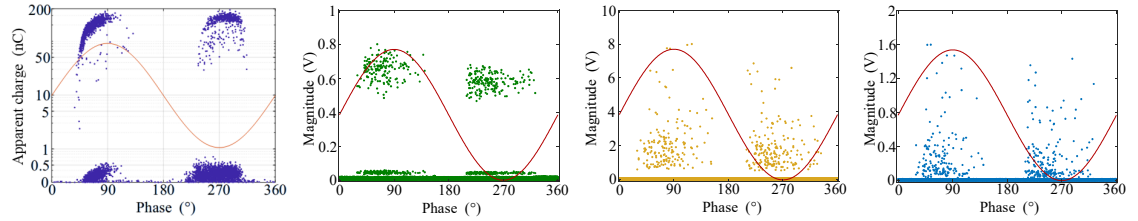


(**a**) Pulse-current (**b**) Ultrasonic (**c**) TEV (**d**) UHF

Figure 12. PRPD pattern of spherical metallic-particle defect at 92.6 kPa and 15 kV (**a**) Pulse-current; (**b**) Ultrasonic; (**c**) TEV; (**d**) UHF.

The patterns obtained from the three online monitoring sensors are considerably sparser than the PRPD pattern measured by the pulse-current method. Among them, the ultrasonic φ–U pattern partially preserves the two-level amplitude structure observed in the reference PRPD pattern. By comparison, the TEV and UHF φ–U patterns do not exhibit a clear separation between the two amplitude populations, indicating relatively limited sensitivity to differences in discharge magnitude.

Figure 13 presents the discharge patterns recorded during the stable PD stage after the metallic sphere had been trapped near one electrode at 22.6 kPa. Compared with the ambient-pressure case, the separation between the upper and lower pulse populations becomes more distinct. The two pulse clusters are no longer connected around the rising and falling portions of the power-frequency voltage waveform, and the lower-amplitude cluster no longer exhibits a highly symmetric distribution. Instead, the discharge pulses become more strongly concentrated around phase angles of approximately 80° and 270°. In addition, the reduction in air pressure leads to a more pronounced difference between the upper pulse clusters.



(**a**) Pulse-current (**b**) Ultrasonic (**c**) TEV (**d**) UHF

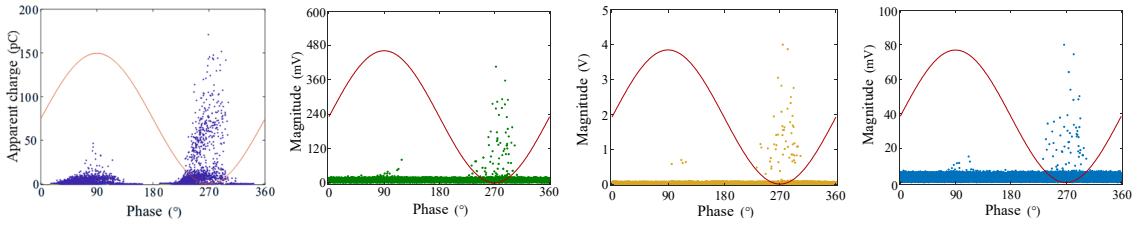
Figure 13. PRPD pattern of spherical metallic-particle defects at 22.6 kPa and 9 kV (**a**) Pulse-current; (**b**) Ultrasonic; (**c**) TEV; (**d**) UHF.

Although the ultrasonic signal undergoes some attenuation under reduced-pressure conditions, the corresponding φ–U pattern still preserves the amplitude-separation feature observed in the PRPD pattern measured by the pulse-current method. By contrast, the φ–U patterns obtained from the TEV and UHF sensors show increased dispersion because the discharge intensities of the upper and lower pulse populations differ more markedly. Even so, these two sensing methods still do not reproduce the amplitude-separation feature of the reference PRPD pattern in a sufficiently distinct manner.

For wire-like metallic particles, PD pattern analysis was performed using the representative configuration in which the longitudinal axis of the wire was approximately aligned with the electric-field direction ($\theta \approx 0^{\circ}$).

Figure 14 presents the PRPD and φ–U patterns of metallic-particle-induced surface discharge on epoxy resin at an applied voltage of 8.5 kV and an ambient pressure of 92.6 kPa. In contrast to the nearly symmetric discharge behavior of the spherical particle, the wire-like particle produces strongly asymmetric phase-resolved discharge characteristics.

As observed in Figure 14a, PD activity occurs in both polarity half-cycles of the power-frequency voltage, whereas the apparent charge magnitude is considerably higher in the negative half-cycle than in the positive half-cycle.

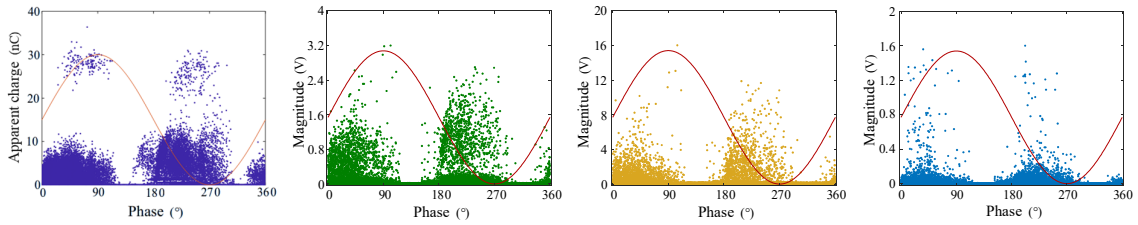


(**a**) Pulse-current (**b**) Ultrasonic (**c**) TEV (**d**) UHF

Figure 14. PRPD pattern of wire-like metallic particle defects at 92.6 kPa and 8.5 kV (**a**) Pulse-current; (**b**) Ultrasonic; (**c**) TEV; (**d**) UHF.

This polarity-dependent behavior can be interpreted in terms of electrostatic induction and the equivalent point-to-plane discharge configuration. During the positive half-cycle, negative charges are induced and concentrated at the wire tip adjacent to the high-voltage electrode. This sharp wire end and the high-voltage electrode therefore constitute an equivalent negative-polarity point-to-plane geometry, with the wire tip acting as the point electrode and the high-voltage electrode as the plane electrode. Conversely, the opposite wire tip and the grounded electrode form an equivalent positive-polarity point-to-plane geometry. Because of the polarity effect in gas discharge, electron emission and subsequent ionization are more readily initiated at a negatively polarized sharp electrode. This behavior generally produces a lower inception voltage, a higher discharge repetition rate, and a greater pulse density. The PRPD characteristics therefore suggest that the wire end facing the high-voltage electrode possesses a stronger tip effect than the opposite end, allowing PD to initiate earlier in the corresponding equivalent point-to-plane discharge region.

At an applied voltage of 15 kV, the discharge develops into a stable PD regime. As illustrated in Figure 15, abundant discharge pulses occur throughout both polarity half-cycles of the power-frequency voltage. Moreover, the φ–U patterns recorded by the ultrasonic, TEV, and UHF sensors show discharge activity around the voltage zero crossings. The PRPD pattern in Figure 15a displays a distinct separation in apparent charge magnitude, similar to the two-level discharge distribution previously observed for the spherical metallic particle.



(**a**) Pulse-current (**b**) Ultrasonic (**c**) TEV (**d**) UHF

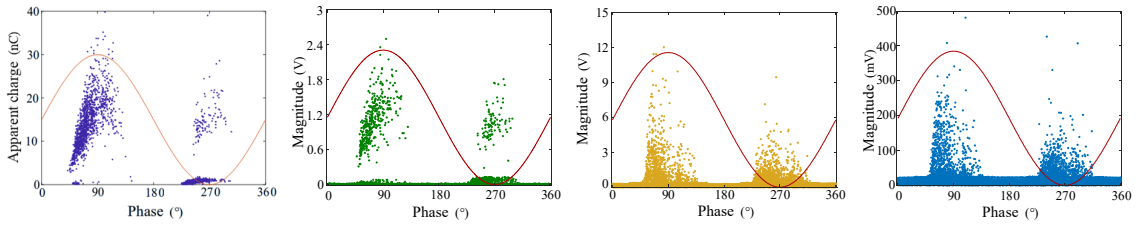
Figure 15. PRPD pattern of wire-like metallic particle defect at 92.6 kPa and 15 kV (**a**) Pulse-current; (**b**) Ultrasonic; (**c**) TEV; (**d**) UHF.

This evolution can be attributed to the substantial increase in the local electric field at both ends of the wire-like particle. At 15 kV, the tip fields considerably exceed the PD inception threshold, leading to strong ionization in the gas gaps between both wire ends and the corresponding electrodes. Consequently, the phase-resolved distribution is markedly more symmetric than the distribution near PD inception. This enhanced

symmetry suggests that, under high electric-field stress, the strong field enhancement imposed by the macroscopic wire geometry dominates the discharge process and effectively suppresses the influence of minor geometric differences between the two wire tips.

Nevertheless, the three online monitoring techniques remain relatively insensitive to differences in discharge magnitude. Although the UHF φ–U pattern shows a certain degree of pulse-amplitude dispersion, none of the three sensors provides sufficient discrimination with respect to apparent charge. In particular, high-intensity PD pulses exceeding 20 nC cannot be clearly separated from lower-intensity pulses below 10 nC in the φ–U patterns measured by the ultrasonic, TEV, and UHF sensors.

Figure 16 presents the PRPD and φ–U patterns recorded under stable surface-discharge conditions for a wire-like metallic-particle defect at 22.6 kPa and an applied power-frequency voltage of 6 kV. As illustrated in Figure 16a, the PRPD pattern measured using the pulse-current method once again exhibits strong phase asymmetry. A large population of high-magnitude discharge pulses is concentrated in the positive half-cycle, whereas the negative half-cycle is dominated by lower-magnitude discharge activity. A limited number of sparse pulses are also observed below 2 nC in the positive half-cycle and above 10 nC in the negative half-cycle.



(**a**) Pulse-current (**b**) Ultrasonic (**c**) TEV (**d**) UHF

Figure 16. PRPD pattern of wire-like metallic particle defects at 22.6 kPa and 6 kV (**a**) Pulse-current; (**b**) Ultrasonic; (**c**) TEV; (**d**) UHF.

This pronounced asymmetry may arise from pressure-dependent breakdown combined with geometric differences between the two wire tips. The reduction in air pressure lowers the critical electric-field strength required for gas breakdown, thereby making the discharge process increasingly sensitive to slight differences in tip sharpness between the two ends of the wire. As a result, the local geometric asymmetry of the particle tips becomes dominant, while the electric-field distortion associated with the overall wire geometry can no longer obscure these morphological differences.

Although the ultrasonic φ–U pattern shows some reduction in signal amplitude under low-pressure conditions, the increased contrast between the discharge sources enables a clear separation of different response-amplitude levels. By comparison, the TEV and UHF sensors successfully detect PD activity but exhibit relatively poor sensitivity to variations in discharge magnitude.

4. Conclusions

The experimental and simulation results show that metallic particles strongly enhance the local electric field on epoxy resin surfaces. Particle geometry determines both the location of the peak field and the preferred discharge-inception region. The maximum field intensity reaches approximately 167.28 times the particle-free value at the metal sphere–epoxy resin–air triple junction for spherical particles and approximately 106.66 times the defect-free value at the tips of wire-like particles. Spherical particles undergo a sequential evolution from PD inception to rolling, electrode capture, and eventual flashover. Wire-like particles exhibit more complex dynamics involving rotation, rolling, and electrode-

directed migration, and their initial orientation exerts a significant influence on both PD development and flashover behavior.

Low pressure substantially aggravates the deterioration of surface insulation associated with metallic-particle defects. When the pressure is reduced from 92.6 to 22.6 kPa, the PDIV of the spherical-particle configuration decreases by approximately 51.6%, from 9.12 to 4.41 kV, whereas the FOV decreases by approximately 23.4%, from 20.60 to 15.77 kV. The markedly larger reduction in PDIV confirms that discharge inception is more pressure-sensitive than flashover. For wire-like particles, the PDIV, PDEV, and FOV all decrease as pressure decreases, and their values depend strongly on the initial particle orientation. Below approximately 42.6 kPa, a fully developed streamer path formed before appreciable particle motion was observed, and the dominant discharge path shifted from surface propagation to direct gas-gap breakdown. Thus, reduced pressure affects not only the discharge threshold but also the dominant insulation failure mechanism.

The multi-sensor measurements further show that ultrasonic, TEV, and UHF techniques can all detect metallic-particle-induced PD at reduced pressure, but differ in their ability to characterize discharge magnitude and pattern evolution. During stable discharge, the spherical-particle defect produces distinct high- and low-magnitude pulse populations. By contrast, the wire-like particle produces greater phase and amplitude asymmetries, both of which vary as pressure decreases. Although ultrasonic signals are attenuated at low pressure, the corresponding φ–U patterns retain relatively clear discrimination between discharge populations of different intensities. TEV and UHF sensing, by comparison, provide reliable event detection but relatively weak discrimination of discharge magnitude. These findings provide experimental support for insulation condition assessment and sensor selection for electrical equipment exposed to high-altitude, low-pressure environments.

Author Contributions: This paper is a result of the collaboration of all co-authors. Formal analysis, W.W.; investigation, Y.C., X.B. and W.W.; methodology, W.W.; software, W.W. and Z.L. (Zhenyu Lu); validation, W.W., K.Z. and Z.L. (Zhixiang Liu); data curation, W.W. and Y.L.; writing—original draft preparation, W.W. and Z.L. (Zhipeng Lei); writing—review and editing, W.W. and Z.L. (Zhipeng Lei); visualization, W.W. and Y.C.; funding acquisition, W.W. and Z.L. (Zhipeng Lei). All authors have read and agreed to the published version of the manuscript.

Funding: This work was supported in part by the Science and Technology Project of State Grid Shanxi Electric Power Co., Ltd., under grants 52053024000U.

Data Availability Statement: The original contributions presented in this study are included in the article. Further inquiries can be directed to the corresponding authors.

Conflicts of Interest: Author Wei Wang, Yinzhang Cheng, Xueting Bai, Zhenyu Lu, Kai Zhang, Yu Liu, Zhixiang Liu was employed by the company State Grid Shanxi Electric Power Company Electric Power Research Institute. The remaining authors declare that the research was conducted in the absence of any commercial or financial relationships that could be construed as a potential conflict of interest. The authors declare that this study received funding from State Grid Shanxi Electric Power Co., Ltd. The funder was not involved in the study design, collection, analysis, interpretation of data, the writing of this article or the decision to submit it for publication.

References

1. Borghei, M.; Ghassemi, M. Insulation materials and systems for more- and all-electric aircraft: A review identifying challenges and future research needs. *IEEE Trans. Transp. Electrif.* **2021**, *7*, 1930–1953. [CrossRef]
2. Li, J.; Wang, Y.H.; Duan, X.H.; Wei, J.W.; Wang, Y.X.; Liang, H.C.; Du, B.X. Surface charging and flashover characteristics of DC-GIS epoxy insulators under AC-DC composite voltage. *IEEE Trans. Dielectr. Electr. Insul.* **2023**, *30*, 787–794. [CrossRef]
3. Li, J.; Wang, Y.H.; Chen, H.; Liang, H.C.; Yao, H.; Zhang, C.; Du, B.X. Polishing orientation affecting surface charging and flashover characteristics of GIL/GIS epoxy spacer. *IEEE Trans. Dielectr. Electr. Insul.* **2022**, *29*, 1625–1632. [CrossRef]

4. Lu, X.S.; Tian, Y.S.; Niu, H.T.; Shi, H.N.; Chen, M.H.; Li, Y.; Fan, B.; Ma, F.Y.; Huang, X.B.; Li, S.T.; et al. Study of electrostatic motion behavior and inhibition of metallic particles in GIS/GIL. *IEEE Trans. Power Deliv.* **2024**, *39*, 83–92. [CrossRef]
5. Niu, B.; Yu, J.Y.; Wang, B.; Ma, F.Y.; Liu, W.F.; Sun, S.P. Research on the influence and suppression technology of micron foreign matter for gas insulated switchgear. *Energy Rep.* **2022**, *8*, 84–93. [CrossRef]
6. Zhu, W.; Dong, Y.; Wang, G.L.; Qiao, Z.T.; Gao, F.Q. High-precision barometric altitude measurement method and technology. In *Proceedings of the 2013 IEEE International Conference on Information and Automation, Yinchuan, China, 26–28 August 2013*; IEEE: New York, NY, USA, 2013; pp. 430–435. [CrossRef]
7. Stone, J.O. Air pressure and cosmogenic isotope production. *J. Geophys. Res. Solid Earth* **2000**, *105*, 23753–23759. [CrossRef]
8. Wang, T.W.; Chen, S.; Xu, E.T.; Zhao, Y.X.; Wang, F.; Xiong, Q.P.; Long, G. Influence of 16–30-kHz sinusoidal voltage on surface discharge characteristics at different pressures. *IEEE Trans. Dielectr. Electr. Insul.* **2025**, *32*, 833–840. [CrossRef]
9. Zhang, G.Q.; Zhang, X.Q.; Wang, B.; Guo, Y.J.; Xiao, S.; Gao, G.Q.; Wu, G.N. Study on the discharge characteristics along the surface of insulating media in the low air pressure and strong airflow environment. *AIP Adv.* **2022**, *12*, 065215. [CrossRef]
10. Riba, J.-R.; Moreno-Eguilaz, M.; Ibrayemov, T.; Boizieau, M. Surface discharges performance of ETFE- and PTFE-insulated wires for aircraft applications. *Materials* **2022**, *15*, 1677. [CrossRef] [PubMed]
11. Shang, X.Y.; Pang, L.; Bu, Q.H.; Zhang, Q.G. Partial discharge aging of epoxy insulation at different high-frequency pulse parameters and environmental stresses. *IEEE Trans. Dielectr. Electr. Insul.* **2025**, *32*, 45–54. [CrossRef]
12. Han, Q.H.; Chen, L.J.; Cotton, I.; Khan, J. Insulating gases for partial discharge management of electrical machines in aerospace applications. *IEEE Trans. Transp. Electrif.* **2023**, *9*, 3590–3600. [CrossRef]
13. Zang, Y.M.; Ghaffarian Niasar, M.; Qian, Y.; Zhou, X.L.; Sheng, G.H.; Jiang, X.C.; Vaessen, P. Optical detection method for partial discharge of printed circuit boards in electrified aircraft under various pressures and voltages. *IEEE Trans. Transp. Electrif.* **2022**, *8*, 4668–4677. [CrossRef]
14. Xu, F.Y.; Zhang, L.K.; Feng, H.; Li, G.C.; Zhu, Y.W.; Wei, Y.H. Research on flashover characteristics and charge evolution mechanism of silicone rubber under different temperature and pressure. *ECS J. Solid State Sci. Technol.* **2025**, *14*, 023009. [CrossRef]
15. Zhang, Z.J.; Jiang, X.L.; Chao, Y.F.; Sun, C.X.; Hu, J.L. Influence of low atmospheric pressure on AC pollution flashover performance of various types of insulators. *IEEE Trans. Dielectr. Electr. Insul.* **2010**, *17*, 425–433. [CrossRef]
16. Zhang, Y.T.; Jin, C.B.; Xin, L.M.; Zhang, P.F.; Wang, H.R.; Tan, S.W.; Liu, P.; Peng, Z.R. Multiscale dynamic simulation study on the adsorption of micrometer-sized metal particles on insulator surfaces for HVDC GIL. *IEEE Trans. Dielectr. Electr. Insul.* **2025**, *32*, 3049–3058. [CrossRef]
17. Gao, Y.H.; Zhang, L.; Zhang, Z.S.; Zhuang, W.J.; Liu, Y.; Liu, B.; Zhang, C.; Li, T.; Wang, X.; Yi, Y.; et al. Metal particle behavior between dielectric-coated electrodes under DC voltage. *IEEE Trans. Dielectr. Electr. Insul.* **2024**, *31*, 2045–2054. [CrossRef]
18. Tian, Z.C.; Li, X.L.; Sun, X.B.; He, J.; Xing, Y. Movement and discharge characteristics of metal dust in GIS under AC voltage: Focus on a special luminescence phenomenon. *IEEE Trans. Dielectr. Electr. Insul.* **2026**, *33*, 723–731. [CrossRef]
19. Jiang, H.; Lai, Y.D.; Gong, Z.Y.; Han, Y.F.; Shao, T. Simulation comparison of the positive and negative surface discharges induced by metal particles in a plate-surface-plate structure under DC excitation in atmospheric air. *J. Phys. D Appl. Phys.* **2024**, *57*, 305202. [CrossRef]
20. Chen, C.; Wang, J.; Wang, J.R.; Li, Z.H.; Guo, R.; Jin, H.; Li, B.T. Numerical simulation research on partial discharge of particle defects at epoxy interface excited by high-frequency sinusoidal voltage. *Polymers* **2023**, *15*, 2320. [CrossRef] [PubMed]
21. Sakai, K.I.; Abella, D.L.; Khan, Y.; Suehiro, J.; Hara, M. Experimental studies of free conducting wire particle behavior between nonparallel plane electrodes with AC voltages in air. *IEEE Trans. Dielectr. Electr. Insul.* **2003**, *10*, 418–424. [CrossRef]
22. Li, X.; Liu, W.D.; Xu, Y.; Ding, D.W. Discharge characteristics and detectability of metal particles on the spacer surface in gas-insulated switchgears. *IEEE Trans. Power Deliv.* **2022**, *37*, 187–196. [CrossRef]
23. Li, X.A.; Wang, S.X.; Hu, X.W.; Zhang, Z.P.; Li, Z.B.; Zhang, Q.G. Improving detection effectiveness of latent metal particles in GIS by applying mechanical impact in power-frequency withstand-voltage test. *IEEE Trans. Power Deliv.* **2024**, *39*, 1023–1030. [CrossRef]
24. Zhang, G.Z.; Chen, X.; Yang, X.; Tian, H.L.; Zhang, J.; Ye, X.M.; Zhang, X.X. Constant voltage-induced intermittent discharge behavior of metal contaminant degradation on the surface of GIS insulators. *IEEE Trans. Dielectr. Electr. Insul.* **2026**, *33*, 2049–2058. [CrossRef]
25. Chen, H.; Wang, H.T.; Zhang, Z.Y.; Guo, R.C.; Han, X.T.; Zhang, X.R.; Li, J.H. A novel composite sensor for UHF partial discharge and gas state measurement in GIS. *IEEE Trans. Instrum. Meas.* **2024**, *73*, 1501410. [CrossRef]
26. Li, Z.; Zang, Y.M.; Wang, C.L.; Tang, Y.S.; Ren, T.; Jiang, X.C. Analysis and diagnosis of optical and UHF partial discharges in GIS based on guided filtering fusion. *IEEE Trans. Dielectr. Electr. Insul.* **2025**, *32*, 2978–2985. [CrossRef]
27. Li, X.; Ding, D.W.; Xu, Y.; Jiang, J.P.; Chen, X.X.; Yuan, M.H. A denoising method for partial discharge ultrasonic signals in GIS based on ultra-high frequency signal synchronization. *IEEE Trans. Power Deliv.* **2024**, *39*, 3316–3325. [CrossRef]

28. Han, X.T.; Wang, H.T.; Sun, Y.; Chen, H.; Meng, X.; Zhou, Y.; Zhang, X.R.; Li, J.H. Partial discharge detection, diagnosis, and location technology based on a novel transient earth voltage-ultrasonic integrated sensor used for switchgear equipment. *Rev. Sci. Instrum.* **2024**, *95*, 084705. [CrossRef] [PubMed]
29. Htet, S.Z.L.; Kondo, T.; Miyake, T.; Khaing, M.T.; Sakoda, T. Partial discharge behavior in epoxy resin including insulation paper. *J. Electrost.* **2026**, *140*, 104242. [CrossRef]

Disclaimer/Publisher's Note: The statements, opinions and data contained in all publications are solely those of the individual author(s) and contributor(s) and not of MDPI and/or the editor(s). MDPI and/or the editor(s) disclaim responsibility for any injury to people or property resulting from any ideas, methods, instructions or products referred to in the content.